ADVANCED FUNCTIONAL MATERIALS
www.afm-journal.de

Materials Views
www.MaterialsViews.com

# Surface State Mediated NIR Two-Photon Fluorescence of Iron Oxides for Nonlinear Optical Microscopy

*Mei-Yi Liao, Cheng-Ham Wu, Ping-Shan Lai, Jiashing Yu, Hong-Ping Lin, Tzu-Ming Liu,* and Chih-Chia Huang**

**The development of fluorescent iron oxide nanomaterials is highly desired for multimodal molecular imaging. Instead of incorporating fluorescent dyes on the surface of iron oxides, a ligand-assisted synthesis approach is developed to allow near-infrared (NIR) fluorescence in $Fe_3O_4$ nanostructures. Using a trimesic acid (TMA)/citrate-mediated synthesis, fabricated $Fe_3O_4$ nanostructures can generate a NIR two-photon florescence (TPF) peak around 700 nm under the excitation by a 1230-nm femtosecond laser. By tailoring the absorption of $Fe_3O_4$ nanostructures toward NIR band, the NIR-TPF efficiency can be greatly increased. Through internal etching, surface peeling, and ligand replacement, spectroscopic results validated that such resonantly enhanced NIR-TPF is mediated by surface states with strong NIR-IR absorption. This TPF signal evolution can be generalized to other iron oxide nanomaterials like magnetite nanoparticles and $\alpha$-$Fe_2O_3$ nanoplates. Using the developed fluorescent $Fe_3O_4$ nanostructures, it is demonstrated that their TPF and third harmonic generation (THG) contrast in the nonlinear optical microscopy of live cells. It is anticipated that the synthesized NIR photofunctional $Fe_3O_4$ will serve as a versatile platform for dual-modality magnetic resonance imaging (MRI) as well as a magnet-guided theranostic agent.**

## 1. Introduction

Magnetic iron oxide nanomaterials have been demonstrated to have great biomedical applications in magnetic resonance imaging (MRI), drug delivery, bioseparation, and hyperthermia.[1,2] Combined with fluorescent nanomaterials, iron oxide nanoparticles can be further engineered with optical properties that facilitate the intracellular monitoring and photomedicine of nanoparticles in vitro or in vivo.[3–6] Drug delivery and pharmacokinetics of nanomedicines can thus be followed from whole body (MRI mode) down to microscopic scale (optical microscopy). Most of these works used composite nanomaterial system to achieve bi-functional (MRI+optical) iron-oxides.[3–6] Their complicated synthesis, quenching by iron oxides, and extra toxicity of dye still impede the wide-spreading use. However, without the integration of fluorescent molecules and inorganic materials on iron oxide surfaces,[5,6] the pure iron oxides themselves do not have fluorescent properties due to a lack of direct transition states.[7,8] The intrinsic magnetic relaxations and local forbidden d–d transitions of the iron oxides prevent their absorption and fluorescence properties.[7,8] Herein, through a ligand-assisted surface modification, we developed an fluorophore-free synthesis method to make iron oxide nanomaterial fluorescent. Using a trimesic acid (TMA)/citrate-mediated synthesis, NIR-TPF can be excited from $Fe_3O_4$ nanostructures. The efficiency of TPF can be greatly increased by tailoring the absorption of $Fe_3O_4$ nanostructures toward NIR wavelength range. Through internal etching, surface peeling, and ligand replacement, we validated that such NIR-TPF was mediated by the ligand-$Fe_3O_4$

Dr. M.-Y. Liao, Prof. P.-S. Lai
Department of Chemistry
National Chung Hsing University
Taichung 402, Taiwan
C.-H. Wu, Prof. T.-M. Liu
Institute of Biomedical Engineering and Molecular Imaging Center
National Taiwan University
Taipei 106, Taiwan
E-mail: tmliu@ntu.edu.tw
Prof. J. Yu
Department of Chemical Engineering
National Taiwan University
Taipei 106, Taiwan
Prof. H.-P. Lin
Department of Chemistry
National Cheng Kung University
Tainan 701, Taiwan
Dr. C.-C. Huang
Biophotonics and Molecular Imaging Research Center
National Yang-Ming University
Taipei 112, Taiwan
E-mail: cchuang-ym@ym.edu.tw

DOI: 10.1002/adfm.201202676

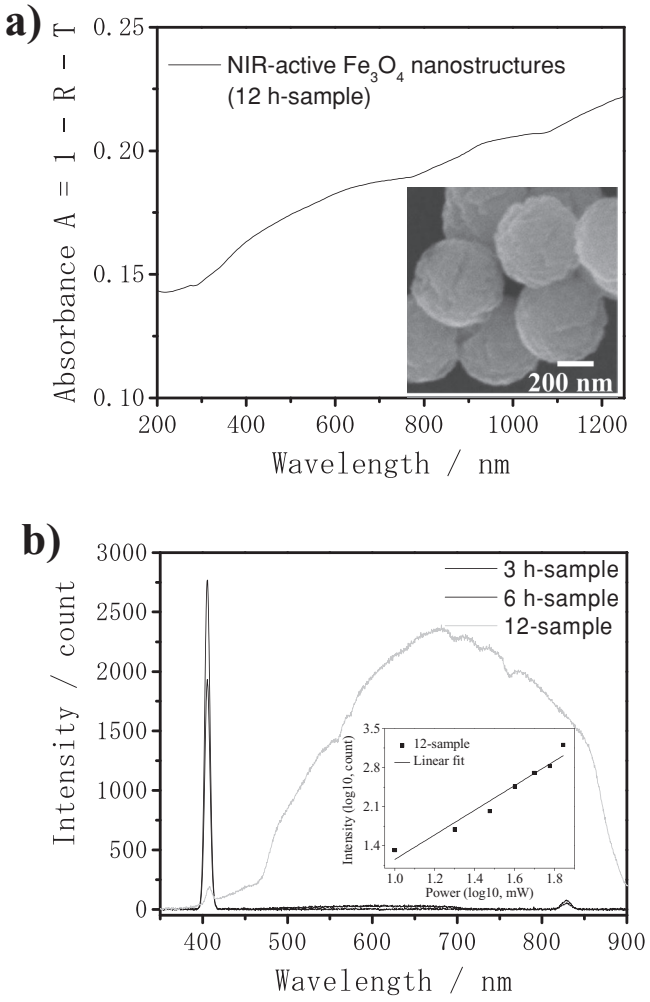


**Figure 1.** a) Absorption spectrum and SEM image (inset) for the 12-h sample. b) Multiphoton NOL spectra and the power dependence of TPF yield (inset) of NIR-active $Fe_3O_4$ particles prepared for different reaction times.

surface states. The generated NIR-TPF extending from 700 nm peak to 900 nm wavelength, at which scattering loss and absorption from endogenous pigments, water, or tissues is greatly reduced.[9–11] It benefits deep-tissue nonlinear optical (NOL) microscopy excited at a least invasive wavelengths (1200–1300 nm).[6,12–14] Finally, we demonstrated that the developed NIR fluorescent $Fe_3O_4$ nanomaterials (sub-micrometer-sized $Fe_3O_4$ (≈440 nm) and nanometer-sized magnetite (≈22 nm)) have readily applied in optical imaging by sufficient TPF and THG contrasts in the NOL microscopy of live cells.

## 2. Results and Discussion

A trimesic acid (TMA)/citrate-mediated synthesis of $Fe_3O_4$ nanostructures can exhibit tunable UV-visible-NIR absorption characteristics and NIR-light induced photothermal therapies.[15] The NIR-active $Fe_3O_4$ particles have ≈440 nm (**Figure 1**a, inset) sizes with a waxberry nanostructure. This was prepared after 12 h of hydrothermal reaction (named as 12-h sample). The absolute absorbance (A) spectrum of 12-h sample was calculated from the reflectance (R) and transmittance (T) values (i.e., A = 1 − R − T) by using a UV-visible-NIR spectrophotometer equipped with an integrating sphere, displaying an enhancement of absorption extending up to 1290 nm (Figure 1a). Exploiting this distinctive NIR-IR absorption feature, we employed a home-built femtosecond (≈100 fs) Cr:forsterite laser, operating at 1230 nm, to excite the nonlinear optical signals in the 12-h sample. The multiphoton NOL spectra of the 12-h sample showed broad multiphoton fluorescence characteristics ranging from 450 to 900 nm (Figure 1b, green). We further analyzed the pump-power dependence of the NIR fluorescence measured at the peak-wavelength (≈700 nm) (the inset of Figure 1b). It displayed a squared dependence of yields on the excitation power, suggesting that the fluorescence in the NIR wavelength is a two-photon excitation process. The emission at shorter wavelength part (450–600 nm) might be coming from three photon fluorescence or upconversion processes. In contrast, samples with weaker NIR absorption (3- and 6-h samples)[15] did not generate noticeable fluorescence. All samples showed a narrow THG peak at ≈410 nm due to refractive index difference between the particles and solutions. We thought this distinctive NIR-TPF behavior resulted from the formation of framework between TMA/citrate and Fe(II)/Fe(III) ions on the surface of the 12-h sample. This framework might cause larger transition probability in the visible-NIR wavelength range due to the evolution of the d–d features of the Fe(II) and Fe(III).

Compared to Au nanorods (with an aspect ratio of ≈3.9 (length 38.2 nm and width 9.8 nm)) (**Figure 2**), Au/Ag nanocage,[13a] and Au NR-in-shell nanostructures,[13b] our photofunctional $Fe_3O_4$ nanostructures (Figure 1a) exhibited more proportion of spectral power in the 700–900 nm wavelength range. This property has potential for detection of fluorescence in deeper tissues.[9,10] It is also worth noting that the preparation of our fluorescent $Fe_3O_4$ nanostructures was based on

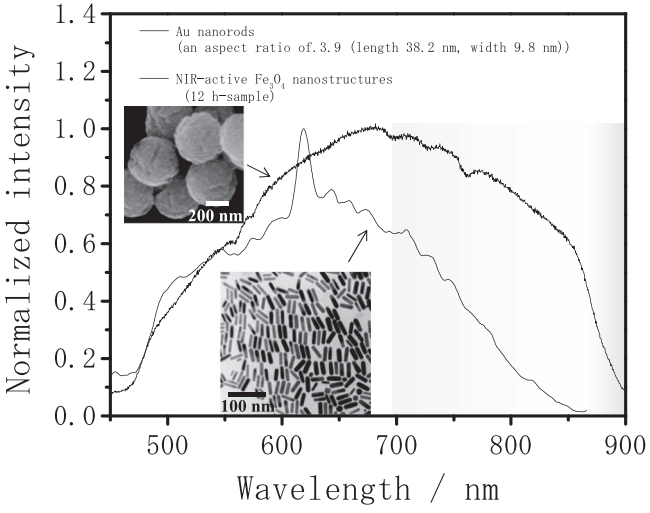


**Figure 2.** Comparison of normalized intensity profiles for NOL spectra of NIR-active $Fe_3O_4$ nanostructures (12-h sample) and Au nanorods under fs excitation at 1230 nm. Their corresponding EM images are inset.

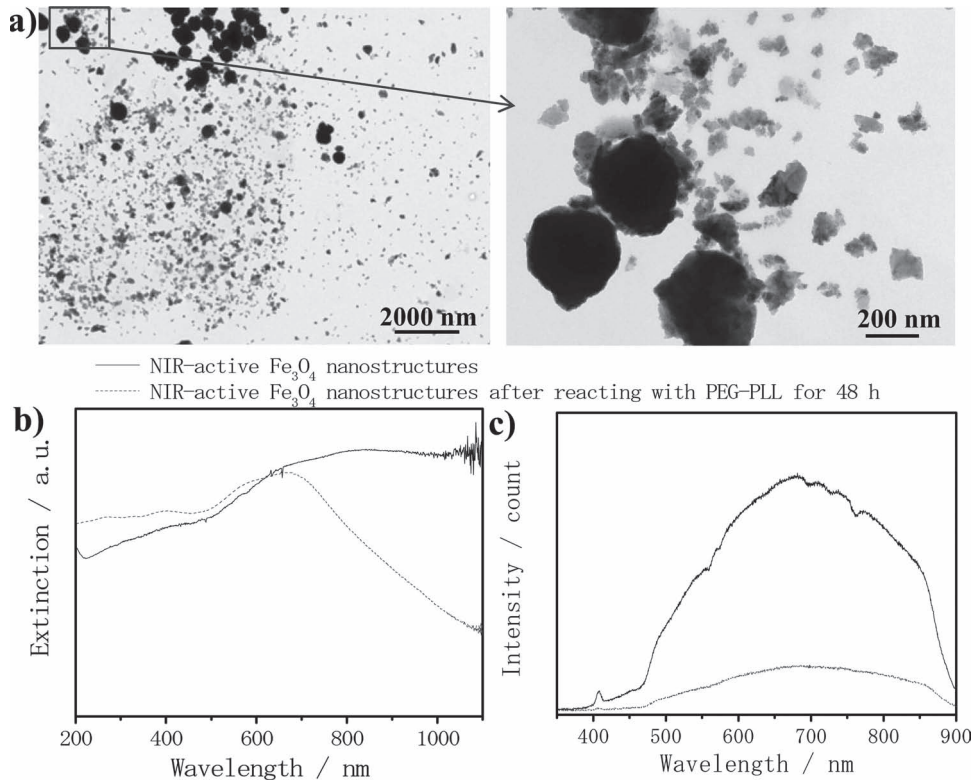


**Figure 3.** a) Absorption and b) NOL spectra for NIR-active $Fe_3O_4$ nanostructures before and after reacting with PEG-PLL polymer for 48 h. c) Low- (left) and high- (right) magnification TEM images for NIR-active $Fe_3O_4$ nanostructures after reacting with PEG-PLL for 48 h.

water phase synthesis, and the particles performed intrinsic magnetic behavior without post-synthesis reaction as well. In contrast, to fabricate Yb-based upconversion nanomaterials combined with superparamagnetism,[6] the yield of Yb-based nanoproducts commonly reacted in the organic phase and followed by complicated chemical modifications, which were less green, toxic, and expensive.

To investigate whether the NIR TPF was dependent on the corresponding long wavelength absorbance, we utilized ligand-exchange process to break the linkages between carboxylate TMA/citrate ligands and iron ions. By reacting with poly(ethylene glycol)-poly(L-lysine) (PEG-PLL) polymer, we found that the surface structures of the bare NIR-active $Fe_3O_4$ particles could be peeled off (**Figure 3**a). The particles' NIR-IR absorption (Figure 3b) decreased and a strong decrease in TPF (Figure 3c) yield was observed after peeling. To demonstrate the successful ligand exchange process, we utilized single lysine amino acid to react with NIR-active $Fe_3O_4$ particles. A consistent result for the surface destruction of bare NIR-active $Fe_3O_4$ particles was observed by TEM image (Supporting Information Figure S2). This verify the $\varepsilon$-amino and carboxyl (C=OOH) groups on the PLL portion of the copolymer plays a crucial role in this ligand exchanging mechanism.

To investigate the contribution of NIR-TPF from $Fe_3O_4$ core, we performed an etching reaction with HCl. As a protection layer, we capped the surface of 12-h sample with APTES-functionalized $mSiO_2$ nanoshells. Particles still keep NIR-IR absorption and NIR-TPF properties. **Figure 4**a,b demonstrated that both the samples' NIR-IR absorption and NIR-TPF bands progressively decreased as the etching time increased. The time-dependent TEM images (Figure 4c and Supporting Information Figure S1) show that the HCl etching process depleted the $Fe_3O_4$ core of the nanocomposite from the inside out. The APTES-functionalized $mSiO_2$ nanoshells prevented TMA/citrate-Fe(II)/Fe(III) frameworks from immediate destruction. The results indicate that majority of the volume of the $Fe_3O_4$ core does not contribute NIR TPF as much as TMA/citrate-Fe(II)/Fe(III) framework (i.e., surface structure) dose.

Then, we investigated the single photon (SP) fluorescence properties of NIR-active $Fe_3O_4$ nanostructures (12-h sample) (**Figure 5**). Peaks at 363, 392, and 615 nm were observed in the fluorescence excitation spectra monitored at 688 nm. Under 615 nm excitation, fluorescence spectrum showed emission peaks at 688, 718, and 756 nm. Excitation at 363 and 392 nm also gave rise to the 688 nm peak. This strong 688 nm SP fluorescence peak was quite close to the peak wavelength of the TPF excited at 1230 nm. That is because the two-photon excitation level exactly matched the energy gap of the 615 nm transition state. Therefore, the substantial TPF yield of the $Fe_3O_4$ nanostructure was resonantly enhanced not only by NIR absorption states but also the absorption band in visible wavelength range.

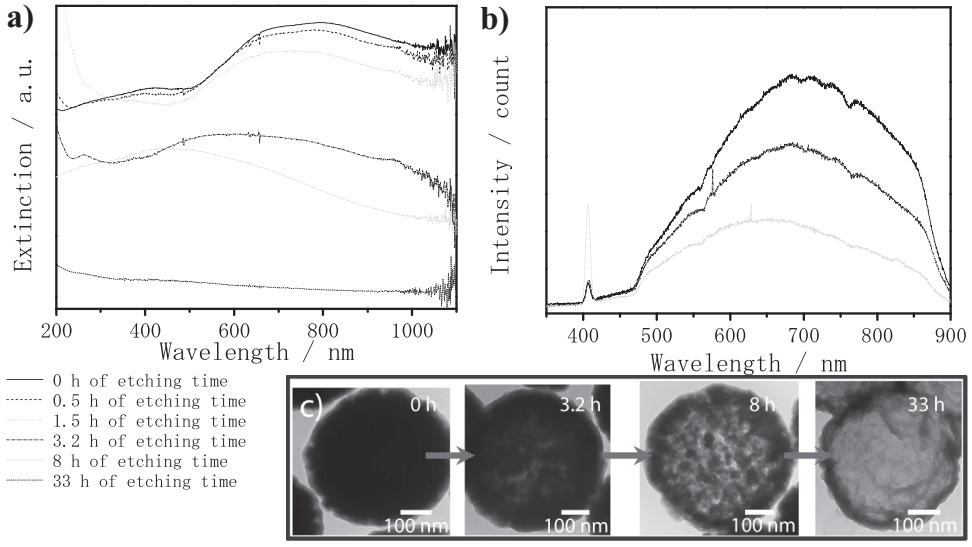


**Figure 4.** Absorption spectra a) NOL spectra, b) TEM images, and c) for the 12-h sample coated with APTES-functionalized $mSiO_2$ nanoshells after HCl etching as a function of etching time.

To gain additional chemical insight regarding these surface states, we measured the O1s spectrum resulting from XPS analysis (**Figure 6**). This provided evidence that carboxylic ligands strongly bound to the surface of the 12-h samples. The O 1s spectrum presented a band at ca. 530.1, 531.7 (shoulder), and ≈533 eV, assigned to the lattice $O^{2-}$ of $Fe_3O_4$,[16] the carboxylate binding to Fe,[17] and the functional groups (COOH, C=O, and –OH groups) form the carboxylic ligands, respectively.[17–19] The surface structures consisted of TMA/citrate ligands coordinated to iron ions, Fe lattices, and O lattices for 12-h sample. According to previous studies,[7,8] the strong overlap between Fe 3d and O 2p orbitals in the distortion of coordination increases the transition probability of spin-forbidden transitions and the relaxation of the Laporte-forbidden transition. Therefore, we suggest that the TMA/citrate ligands coordinated to iron ions of 12-h sample may affect the surface states of the $Fe_3O_4$ particles and create new emission centers on the surface for electron-hole recombination.

Based on the results shown above, we can validate that the TPF of the 12-h sample was highly correlated to the efficient NIR-IR absorption, induced by the corresponding surface structures and states. Additional supporting experiments by changing Fe(III)/Fe(II) ratios and replacing TMA ligands with terephthalic acid, phthalic acid, and benzoic acid were performed. The NIR-IR absorption, irrespective of the ligand type, is still critical for the efficient generation of NIR-TPF in $Fe_3O_4$ nanostructures (Supporting Information Figure S3 and Figure S4).

Obviously, this critical NIR-IR absorption is due to the iron ions and it is commonly observed for the Fe-doped minerals of silicate glasses[20] and tourmalines.[21] The photon absorption

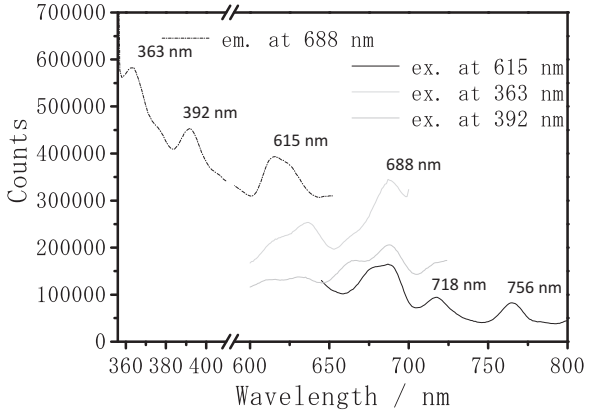


**Figure 5.** Single-photon fluorescence spectra of 12-h sample.

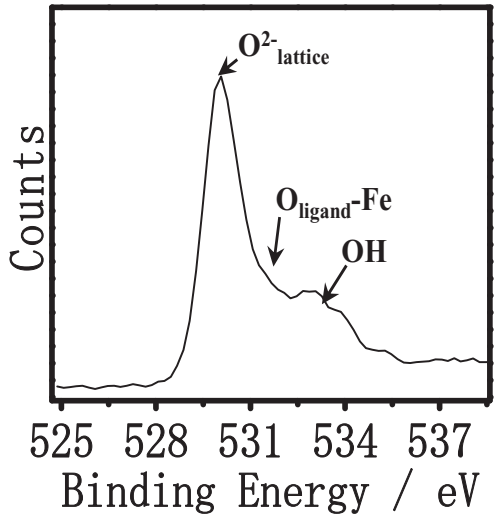


**Figure 6.** XPS spectra of NIR-active $Fe_3O_4$ nanostructures (12-h sample).

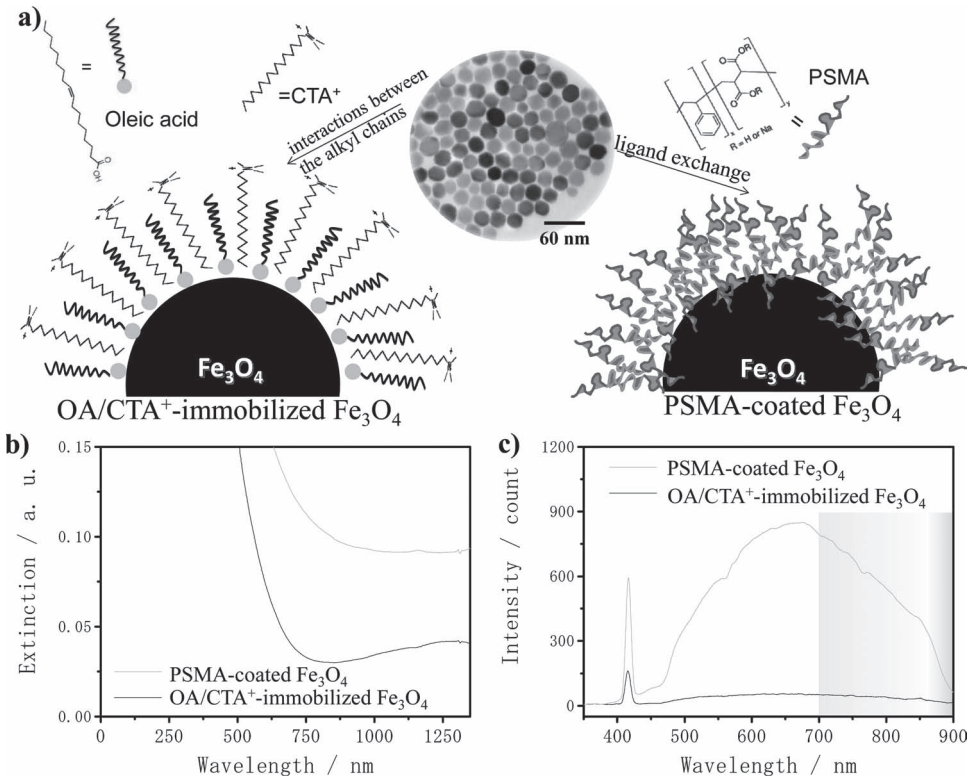


**Figure 7.** a) Scheme illustrated the as-prepared pure magnetite ($Fe_3O_4$) nanoparticles (22 nm) were capped with OA for the preparation of PSMA-coated and OA/$CTA^+$-immobilized $Fe_3O_4$ nanoparticles (22 nm in core size). b) Absorption spectra and c) NOL spectra for PSMA-coated and OA/$CTA^+$-immobilized $Fe_3O_4$ nanoparticles.

in the d-d transition states of Fe ions improved in ligand fields when the Fe ions were located at the disorder coordination structure. Furthermore, previous reports indicated the capping ligands strongly affect the absorption properties of $Fe_2O_3$ and $Fe_3O_4$ nanoparticles.[22] Reimhult and co-workers examined the surface structures of $Fe_3O_4$ nanoparticles capped with catechol derivatives by electron paramagnetic resonance (EPR) spectroscopy and observed the $Fe^{3+}$ to exhibit a distorted ligand field.[23] In this context, we adopted solution systems which proved that the TMA and citrate ligands bond to Fe(II) ions promoting the NIR absorbance.[15]

Regarding the mechanism of energy relaxation, for example $Mn^{2+}$ ion doped ZnSe quantum dots[24] and $NaYF_4$: Yb/Er nanoparticles,[25] a new energy transition of $^4T_1 \rightarrow {}^6A_1$ level in the host materials has been suggested to contribute photon emission. As a result, the two types of energy levels that possibly allowed excitons to recombine in NIR-active $Fe_3O_4$ nanostructures were i) d-d bands,[11,24,25] which involved ≈1200 nm (NIR) by $Fe^{2+}$ ions and 600–900 nm by $^6A_1 \leftrightarrow {}^4T_1$ (NIR) + $^4T_2$ (visible) of $Fe^{3+}$ ions,[7,20] and ii) another band possibility related to surface defects and surface trapping states,[8b,c] which usually occurs in the luminescent nanomaterials.[26]

We thought that this surface-state mediated NIR-TPF can be generalized to other NIR-IR active iron oxide nanomaterials when their surfaces are coated with poly-carboxylate molecules. To prove the feasibility, we examined the NOL properties of pure magnetite (stoichiometric $Fe_3O_4$: $[Fe^{3+}][Fe^{2+}Fe^{3+}]O_4$) nanoparticles (**Figure 7**) and $\alpha$-$Fe_2O_3$ nanoplates (Supporting Information Figure S5). Previous reports have indicated that the pure magnetite possesses an intervalence charge transfer (IVCT) covering to NIR-IR region.[7a,c] The chemical purity of 22-nm truncated octahedral magnetite nanoparticles with oleic acid (OA) protection was prepared following our previous synthesis method.[27,28] After implementing different surface modification strategies (Figure 7a),[27] we found that the absorption at 1230 nm of the poly(styrene-alt-maleic acid) (PSMA)-coated magnetite nanoparticles was ≈2.2 times higher than that of the OA/cetyltrimethylammonium ($CTA^+$)-immobilized nanoparticles (Figure 7b). PSMA polymer rendered rich–COOH groups which would be subsequent affecting the surface structure of magnetite nanoparticles. Accordingly, the multiphoton NOL spectra showed that the NIR-TPF for PSMA-coated magnetite nanoparticles was stronger than that for the OA/$CTA^+$-immobilized nanoparticles (Figure 7c). The color highlight between 700 and 900 nm in Figure 7c represented the TPF coverage in the NIR region. On the other hand, the NIR-active $\alpha$-$Fe_2O_3$ nanoplates also exhibited good TPF behavior (Supporting Information Figure S5).

**Figure 8** shows the relationship of iron oxides' molar extinction coefficient $\varepsilon$ at an IR wavelength of 1230 nm and NIR-TPF intensity. The plots indicate that the yield of NIR-TPF is nearly linearly dependent on its intrinsic $\varepsilon$ value. This again confirms that the key for NIR-TPE of $Fe_3O_4$ nanostructures is NIR absorption of surface states.

Finally, we investigated the biocompatibility of photofunctional $Fe_3O_4$ and their application for TPF microscopy. The cytotoxicity results of particles[15,27,28] and free capping ligands (Supporting

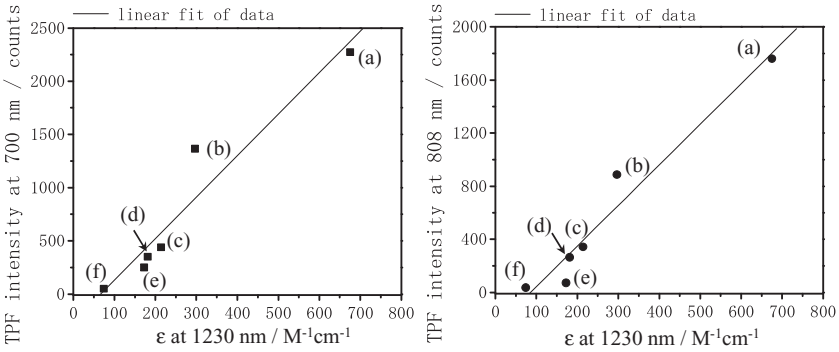


**Figure 8.** Relationship between molar extinction coefficient $\varepsilon$ at 1230 nm and NIR-TPF intensity at 700 nm (left) and 808 nm (right) for a) as-prepared iron oxides materials (120 ppm Fe; 12-h sample, b) as-synthesized iron oxide with a Fe(III)/Fe(II) ratio at 1/9, c) 12-h sample after reacting with PEG-PLL for 48 h, d) as-synthesized iron oxide with a Fe(III)/Fe(II) ratio at 2/8, e) $\alpha$-$Fe_2O_3$ nanoplates, and f) OA/$CTA^+$-immobilized $Fe_3O_4$ nanoparticles.

Information Figure S6) have good biocompatible in vitro. Then, we treated live A549 lung cancer cells with the 12-h sample overnight. The particles were taken up by cells, which was easily confirmed by bright field microscopy. Subsequently, we imaged these live cells with multiphoton nonlinear microscopy to demonstrate the feasibility of using 12-h samples as a TPF contrast agent. The detailed structure of the imaging system has been described elsewhere.[12a] After exposing these particle-treated cells for 15 min with a 20 mW, 1230 nm laser, strong THG (**Figure 9**a, magenta color) and NIR TPF (Figure 9b, yellow color) contrasts were observed within the cytoplasm. Granules of strong THG contrast indicate the distribution of endocytosed iron oxides. Some of these granules did not emit NIR-TPF, which might be due the effects of low-pH values or enzymes on their surface states. We observed no obvious changes in cellular morphology or apoptosis events during imaging. Importantly, photobleaching was absent as well. In contrast, cells that did not receive particle treatment had no TPF signals, and only weak THG signals were observed (Figure 9d). For the particle-treated cells, vesicles that encapsulated $Fe_3O_4$ provided strong THG contrast, and the particles were able to generate sufficiently strong nonlinear contrasts (Figure 9c), which could not be observed in cells that did not receive particle treatment. PSMA-coated magnetite nanoparticles were also readily applied for cellular imaging with a NOL microscopy (Supporting Information Figure S7). Both NIR-active $Fe_3O_4$ nanostructures (12-h sample) and PSMA-coated magnetite nanoparticles-treated cells revealed higher signal intensity than that from untreated cells with the same applied voltage and integration time, indicating an efficient optical probe for cell imaging. These results confirmed the safety and contrast performance of the NIR-active $Fe_3O_4$ nanostructures in cells.

## 3. Conclusions

Without using fluorescence dyes, we demonstrated a ligand-assisted synthesis method to make iron oxide fluorescent in NIR region. Using selective surface etching, we validated that the surface-related NIR transition state was the main factor responsible for two-photon fluorescence. Excited with an infrared (1230 nm) femtosecond laser, this NIR-TPF provides sufficient contrast for NOL microscopy in live cells. This strategy of surface-state mediated NIR TPF can be generalized to other iron oxide nanomaterials with smaller particle sizes. Multiple scale molecular imaging with fluorescent iron oxides can thus be realized without the integration of toxic fluorescent dyes. We also showed that the NIR-active $Fe_3O_4$ particles (≈440 nm) were porous in structure and could be loaded with a DOX anticancer drug. These results suggest a new concept regarding the potential application of all-NIR $Fe_3O_4$ systems to integrate magnetic and fluorescence characteristics for the development of a theragnosis drug delivery platform. The

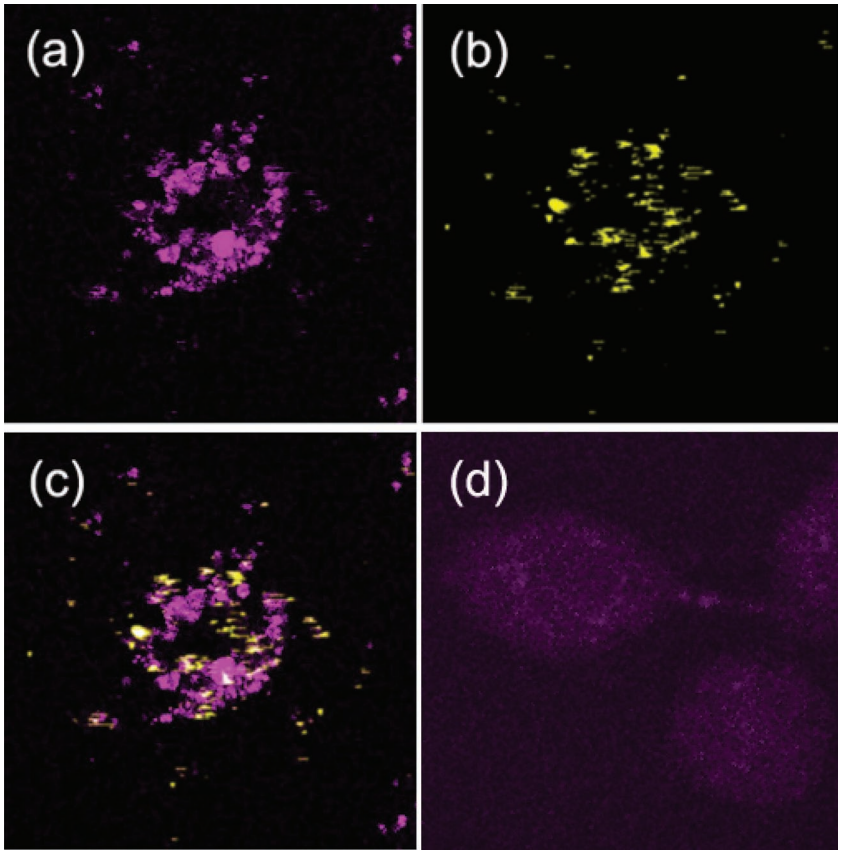


**Figure 9.** a) THG microscopy, b) TPF microscopy, and c) combined images of $Fe_3O_4$ particle (12-h sample) treated A549 lung cancer cells. d) THG and TPF combined images of A549 lung cancer cells without particle treatment.

used of an NIR laser to trigger drug release will be reported in the near future.

## 4. Experimental Section

*Materials*: Iron(II) chloride tetrahydrate ($FeCl_2{\cdot}4H_2O$, 99–102%) (Merck), trisodium citrate (100%, J. T. Baker), benzene-1,3,5-tri-carboxylic acid (trimesic acid (TMA), 98%) (Alfa Aesar), benzoic acid (Sigma-Aldrich), benzene-1,4-dicarboxylic acid (terephthalic acid, >98%) (Alfa Aesar), benzene-1,2-dicarboxylic acid (phthalic acid, 99.5%) (Alfa Aesar), sodium hydroxide (NaOH, 99% 0 (Riedel-de Haën), aminopropyl-triethoxysilane (APTES, 99%) (Acros), tetraethyl orthosilicate (TEOS, 98%) (Acros), ethanol (EtOH, 99.9%) (J. T. Baker), poly(styrene-alt-maleic acid) sodium salt (PSMA, 13 wt% solution in water (Aldrich), and cetyltrimethylammonium bromide (CTAB, >99%) (Acros) were purchased and used without further purification.

*Preparation of the NIR-activated Iron Oxide Nanostructure*: The preparation of the NIR-activated $Fe_3O_4$ nanostructures was described in our previous report.[15] $FeCl_2{\cdot}4H_2O$ (10 mL, 50 mM), TMA (4.5 mL, 25 mM), NaOH (18 mg), and trisodium citrate (0.15 g) were mixed by stirring and then immediately transferred to a 23-mL Teflon-lined stainless steel autoclave to be heated at 200 °C for 12 h. At different reaction times (3, 6, and 12 h), the hydrothermal process was stopped by cooling the solution to room temperature to collect the synthesized materials by centrifugation. A centrifugation-washing process with deionized water was repeated three times to purify the synthesized iron oxide products.

This synthesis method to fabricate the iron oxide nanomaterials with different $FeCl_2$ and $FeCl_3$ precursor ratios was described in previous reports.[15] With precursor concentrations and amounts (metal and ligand ions) identical to those used for the preparation of the NIR-activated $Fe_3O_4$ nanostructures (12-h sample) above, we adjusted the ratios of the $Fe(II)Cl_2$ and $Fe(III)Cl_3$ precursors and used the same amounts of trisodium citrate (0.15 g) and TMA (4.5 mL, 25 mM) molecules in a hydrothermal reaction at 200 °C for 12 h. After 12 h, a centrifugation-washing process with deionized water was repeated three times to purify the synthesized iron oxide products.

The synthesis of iron oxide nanostructures assisted by various ligands (i.e., citrate/terephthalic acid-, citrate/benzoic acid-, and citrate/phthalic acid-mediated hydrothermal reactions) were carried out. The ligands of terephthalic acid, benzoic acid, and phthalic acid were utilized to replace TMA ligands for the control experiments. After 12 h of reaction, a centrifugation-washing process with deionized water was repeated three times to purify the synthesized iron oxide products.

*Preparation of the NIR-Activated $Fe_3O_4$@mSiO$_2$ Nanostructures*: The mesoporous silica-coated strategy to prepare $Fe_3O_4$@mSiO$_2$ (mSiO$_2$ = mesoporous silica) nanostructure was synthesized as described in the previous strategy[28,29] with a slight modification: 0.86 mL of the NIR-activated $Fe_3O_4$ nanostructure (12-h sample) (1800 ppm [Fe]) after 12 h of hydrothermal reaction and purification was dispersed in 4.575 mL of a CTAB (5.46 mM) and NaOH solution (1.37 mM) in a 20 mL glass vial. A continuous Ar flow was applied to the vial to eliminate air. Next, 0.026 mL of TEOS was added to the mixture under ultrasonic treatment in a sonication bath at 55 °C. The reaction glass vial was enclosed with a foil-lined urea screw cap in the Ar environment. After 2 h of reaction, the resulting black solution was collected by centrifugation and washed 3 times with distilled water. Using an APTES/ethanol extraction, the CTAB was removed from the mesoporous silica shells of the $Fe_3O_4$@mSiO$_2$ nanostructures. Then, 1.55 mg[Fe] of the $Fe_3O_4$@mSiO$_2$ nanostructures was suspended in ethanol in the sonication bath at 80 °C in the 20 mL glass vial with a continuous Ar flow. Subsequently, 84 µL of APTES was added to yield the APTES-functionalized $Fe_3O_4$@mSiO$_2$ nanostructures (referred to as NIR-activated nanocomposites). The reaction glass vial was enclosed with a foil-lined urea screw cap in the Ar environment. After the interaction (6 h) of mesoporous silica nanoshells with the APTES molecules under ultrasonic treatment in the sonication bath at 80 °C, the black product was collected by a centrifugation/re-suspension process more than 3 times and washed with ethanol.

*Preparation of the NIR-Activated $\alpha$-$Fe_2O_3$ Nanostructures*: Following the previous synthesis[15] with $\gamma$-$Fe_2O_3$ nanoparticles as the iron(III) source, 10 mL of water, including $\gamma$-$Fe_2O_3$ nanoparticles (0.345 mol), 4.5 mL of TMA (25 mM), 18 mg of NaOH, and 0.15 g of sodium citrate were mixed by stirring and then immediately transferred to a 23-mL Teflon-lined stainless steel autoclave, and the reaction was heated at 200 °C for 24 h. The washing and purification processes were followed according to the above description.

*Preparation of the Pure Magnetite (Stoichiometric $Fe_3O_4$: [$Fe^{3+}$][$Fe^{2+}Fe^{3+}$] $O_4$) Nanoparticles*: Using a previously reported synthesis method,[27,28] the OA-coated magnetite nanoparticles (22-nm in diameter) were prepared through the thermal decomposition of iron acetylacetonate, $Fe(acac)_3$, in the presence of oleic acid and trioctylamine. For PSMA polymer coating, a ligand exchange method using polyelectrolyte PSMA with rich –COOH groups was employed to replace hydrophobic oleic ligands, like previous reports on poly(acrylic acid) (PAA).[30] The polystyrene fractions of PSMA polymers via $\pi$–$\pi$ interaction between the aromatic groups[31] would be embedded within hydrophilic –COOH/–$COO^-$ groups to ensure the improvement of particle solubility in $H_2O$. By CTA coating, the Van der Waals interactions between the alkyl chains in oleic acid and $CTA^+$ was utilized to synthesize OA/$CTA^+$-immobilized $Fe_3O_4$ nanoparticles,[27] where the hydrophilic charged head groups of CTAB extended outward.

*Cytotoxicity Analysis*: For the MTT assay,[27–29] an A549 (human alveolar basal epithelial cancer cells) cell line (8000 cells/well) was cultured in a 96-well microplate with 100 µL of Dulbecco's modified Eagle's medium (DMEM) containing 10% fetal bovine serum (FBS) at 37 °C in 5% $CO_2$/95% air for 1 day. TMA and trisodium citrate were loaded separately into 96-well microplates with various concentrations (0–250 µg/ml) one day after they had been cultured. The culture medium was then removed and replaced with 100 µL of the new culture medium containing 10% MTT reagent. The cells were then incubated for 4 h at 37 °C to allow the formazan dye to form. The culture medium in each well was then removed, and dimethyl sulfoxide (DMSO) (200 µL/well) was added for an additional 10 min of incubation. After the cells were centrifuged, the resulting formazan in each well was transferred to an ELISA plate. The quantification determining cell viability was performed using optical absorbance (540/650 nm) and an ELISA plate reader.

*Nonlinear Microscopic Imaging*: A human lung carcinoma cell line (A549) was cultured in Dulbecco's modification of Eagle's medium (DMEM, Cellgro) plus 10% fetal bovine serum (FBS, Gem Cell) at 37 °C under 5% $CO_2$. The cells were collected by trypsinization, placed onto a 10-cm tissue culture Petri dish, and allowed to grow for 3 days.

To evaluate the two-photon fluorescence contrast, the A549 cells were treated with $Fe_3O_4$ nanostructures and incubated with the cells at least 12 h for uptake. The imaging system is a femtosecond laser based multiphoton nonlinear optical microscope with sub-micrometer 3D spatial resolution. The laser wavelength was approximately 1230 nm, which falls in the NIR penetration window (1200–1300 nm) of most biological tissues. Compared with the commonly used Ti:sapphire laser (700–1000 nm), this wavelength does not two-photon resonantly excite the Soret band of many endogenous fluorophores in cells and tissues and thus, causes the least on-focus damage. Give its advantages for in vivo imaging in deep tissues, it has been widely applied in studies of developmental biology[12a] and in human clinical use.[12b,c] Because most autofluorescence is suppressed, the optical contrast agents that can efficiently excite at approximately 615 nm have high contrast and benefit deep tissue imaging. The laser beam was XY-scanned by a scanning unit (FV300, Olympus) cascaded with an inverted microscope (IX71, Olympus). The laser beam transmitted a multiphoton dichroic beam splitter (edged at 665 nm) and was focused using a water immersion objective (NA = 1.2, 60×, Olympus). The generated two-photon fluorescence (TPF), second harmonic generation (SHG), and third harmonic generation (THG) were epi-collected by the same objective. The TPF signals (>665 nm) transmit a dichroic beam-splitter and were detected by a photomultiplier tube (PMT) in a scanning unit. The SHG and THG signals were reflected and then separated by another dichroic beam splitter edged at 490 nm. They were detected separately by two other PMTs (R928, Hamamatsu). The detection sensitivity of PMT for THG signal is four times higher

than that for TPF signals. To raise the signal level of weak THG, applied eight-times higher gain than TPF channel was applied. All three signal channels were reconstructed to 512 × 512 images with software in computer with a 2 Hz frame rate. To image the live cells, a micro-incubator on a microscope was used to create an environment with a temperature of 37 °C in an environment that was 5% $CO_2$/95% air. The temperature of the thermostat (LAUDA Ecoline Staredition RE 204) was set to 50 °C to achieve 37 °C at the distal ends of objective, but the vapor reaching the micro-incubator through the duct maintained the micro-incubator at approximately 37 °C. The gas controller (OkO Lab) continuously supplied 5% $CO_2$, and maintained the outlet absolute pressure at 1 atm. The water immersion objective with 1.2 NA was heated by a dual temperature controller (TC-144, Warner Instruments). This made the temperature at the bottom of the dish that contacted the objective approximately 37 °C.

*Characterization*: Electron microscopy images were obtained using transmission electron microscopes (JEOL 3010 at 300 KV and PHILIPS CM-200 at 200 KV). Field emission scanning electron microscope (FESEM) images of the nanoshells on the Cu plate substrates were taken using an FE-SEM at 10 kV (XL-40 FEG; Philips). A UV-visible-NIR diffuse reflectance spectrophotometer (JASCO V-670, Japan) equipped with an integrating sphere were used to record absolute absorbance characteristics of samples in the wavelength ranges of 190–1290 nm. A UV-Vis spectrophotometer (8452A; Hewlett-Packard Company, Palo Alto, CA) was used to immediately and temporally measure the extinction optical of samples in the wavelength ranges of 190–1100 nm. The emission of the NIR-activated $Fe_3O_4$ nanostructures was measured using a FSP 920 Fluorescence spectrophotometer (Edinburgh Instruments, UK), with wavelengths ranging from 356 to 800 nm. The Fe ions were quantified using an inductively coupled plasma atomic emission spectrometer (ICP-AES, JY138 Spectroanalyzer; Horiba Jobin Yvon, Inc., Edison, NJ). The sample concentration was approximately 120 ppm [Fe] as measured in the nonlinear spectra.

## Supporting Information

Supporting Information is available from the Wiley Online Library or from the author.

## Acknowledgements

M.-Y.L. and C.-H.W. contributed equally to this work. This work was supported by the National Science Council (NSC 100-2628-E-002-006 and NSC 101-2113-M-010-002-MY2) and National Health Research Institutes (NHRI-EX101-10114EC), Taiwan. The laser system was supported by the National Health Research Institutes under grant number NHRI-EX101-9936EI.

Received: September 15, 2012
Revised: October 29, 2012
Published online: November 21, 2012

[1] J. Xie, G. Liu, H. S. Eden, H. Ai, X. Chen, *Acc. Chem. Res.* **2011**, *44*, 883.
[2] C. S. S. R. Kumar, F. Mohammad, *Adv. Drug Delivery Rev.* **2011**, *63*, 789.
[3] C. Wang, J. Chen, T. Talavage, J. Irudayaraj, *Angew. Chem. Int. Ed.* **2009**, *48*, 2759.
[4] C. Wang, C. Xu, H. Zeng, S. Sun, *Adv. Mater.* **2009**, *21*, 3045.
[5] Y.-S. Lin, S.-H. Wu, Y. Hung, Y.-H. Chou, C. Chang, M.-L. Lin, C.-P. Tsai, C.-Y. Mou, *Chem. Mater.* **2006**, *18*, 5170.
[6] a) L. Cheng, K. Yang, Y. Li, J. Chen, C. Wang, M. Shao, S.-T. Lee, Z. Liu, *Angew. Chem. Int. Ed.* **2011**, *50*, 7385; b) F. Chen, S. Zhang, W. Bu, X. Liu, Y. Chen, Q. He, M. Zhu, L. Zhang, L. Zhou, W. Peng, J. Shi, *Chem. Eur. J.* **2010**, *16*, 11254; c) J. Shen, L.-D. Sun, Y.-W. Zhang, C.-H. Yan, *Chem. Commun.* **2010**, *46*, 5731.
[7] a) Y. P. He, Y. M. Miao, C. R. Li, S. Q. Wang, L. Cao, S. S. Xie, G. Z. Yang, B. S. Zou, *Phys. Rev. B: Condens. Matter Mater. Phys.* **2005**, *71*, 125411; b) T. Hashimoto, T. Yamada, T. Yoko, *J. Appl. Phys.* **1996**, *80*, 3184; c) R. M. Cornell, U. Schwertmann, *The Iron Oxides: Structure, Properties, Reactions, Occurrence and Uses*, Wiley-VCH, Weinheim **2003**.
[8] a) G. Chatzikyriakos, K. Iliopoulos, A. Bakandritsos, S. Couris, *Chem. Phys. Lett.* **2010**, *493*, 314; b) D. A. Wheeler, G. Wang, Y. Ling, Y. Li, J. Z. Zhang, *Energy Environ. Sci.* **2012**, *5*, 6682; c) B. Zou, W. Huang, M. Han, S. F. Y. Li, X. Wu, Y. Zhang, J. Zhang, P. Wu, R. Wang, *J. Phys. Chem. Sol.* **1997**, *58*, 1315; d) B. S. Zou, V. Volkov, *J. Phys. Chem. Solids* **2000**, *6*, 757.
[9] a) C.-K. Sun, S.-W. Chu, S.-Y. Chen, T.-H. Tsai, T.-M. Liu, C.-Y. Lin, H.-J. Tsai, *J. Struct. Biol.* **2004**, *147*, 19; b) S.-Y. Chen, S.-U. Chen, H.-Y. Wu, W.-J. Lee, Y.-H. Liao, C.-K. Sun, *IEEE J. Sel. Top. Quantum Electron.* **2010**, *16*, 478; c) S.-Y. Chen, H.-Y. Wu, C.-K. Sun, *J. Biomed. Opt.* **2009**, *14*, 060505.
[10] a) R. Weissleder, *Nat. Biotechnol.* **2001**, *19*, 316; b) V. J. Pansare, S. Hejazi, W. J. Faenza, R. K. Prud'homme, *Chem. Mater.* **2012**, *24*, 812.
[11] Y. Zhang, G. Hong, Y. Zhang, G. Chen, F. Li, H. Dai, Q. Wang, *ACS Nano* **2012**, *6*, 3695.
[12] a) P. C. Ray, *Chem. Rev.* **2010**, *110*, 5332; b) W. R. Zipfel, R. M. Williams, W. W. Webb, *Nat. Biotechnol.* **2003**, *21*, 11; c) S. H. Nalwa, *Adv. Mater.* **1993**, *5*, 341.
[13] a) L. Tong, C. M. Cobley, J. Chen, Y. Xia, J.-X. Cheng, *Angew. Chem. Int. Ed.* **2010**, *49*, 3485; b) K. W. Hu, T. M. liu, K.-Y. Chung, K. S. Huang, C. T. Hsieh, C. K. Sun, C. S. Yeh, *J. Am. Chem. Soc.* **2009**, *131*, 14186.
[14] a) P. Gerner, C. Reinhard, H. U. Güdel, *Chem. Eur. J.* **2004**, *10*, 4735; b) W. Wei, T. He, X. Teng, S. Wu, L. Ma, H. Zhang, J. Ma, Y. Yang, H. Chen, Y. Han, H. Sun, L. Huang, *Small* **2012**, *8*, 2271.
[15] M.-Y. Liao, P.-S. Lai, H.-P. Yu, H.-P. Lin, C.-C. Huang, *Chem. Commun.* **2012**, *48*, 5319.
[16] T. Yamashita, P. Hayes, *Appl. Surf. Sci.* **2008**, *254*, 2441.
[17] C. Han, Q. Liu, D. G. Ivey, *Electrochim. Acta* **2008**, *53*, 8332.
[18] L. H. Dubois, B. R. Zegarski, R. G. Nuzzo, *Langmuir* **1986**, *2*, 412.
[19] S. Stepanow, T. Strunskus, M. Lingenfelder, A. Dmitriev, H. Spillmann, N. Lin, J. V. Barth, C. Wöll, K. Kern, *J. Phys. Chem. B* **2004**, *108*, 19392.
[20] a) M. Yamashita, T. Akai, R. Sawa, J. Abe, M. Matsumura, *J. Non-Cryst. Solids* **2008**, *354*, 4534; b) B. Hannoyer, M. Lenglet, J. Dürr, R. Cortes, *J. Non-Cryst. Solids* **1992**, *151*, 209; c) R. K. Kulladapu, H. Li, G. L. Smith, J. D. Crum, J.-S. Jeoung, W. H. Poisl, M. C. Weinberg, *J. Non-Cryst. Solids* **2003**, *317*, 301.
[21] P. B. Merkel, C. M. Breeding *Gems Gemol.* **2009**, 112.
[22] a) M. D. Shultz, J. U. Reveles, S. N. Khanna, E. E. Carpenter, *J. Am. Chem. Soc.* **2007**, *129*, 2482; b) C. Xu, K. Xu, H. Gu, R. Zheng, H. Liu, X. Zhang, Z. Guo, B. Xu, *J. Am. Chem. Soc.* **2004**, *126*, 9938.
[23] E. Amstad, H. k. Fischer, A. U. Gehring, M. Textor, E. Reimhult, *Chem. Eur. J.* **2011**, *17*, 7396.
[24] S. Acharya, D. D. Sarma, N. R. Jana, N. Pradhan, *J. Phys. Chem. Lett.* **2010**, *1*, 485.
[25] G. Tian, Z. Gu, L. Zhou, W. Yin, X. Liu, L. Yan, S. Jin, W. Ren, G. Xing, S. Li, Y. Zhao, *Adv. Mater.* **2012**, *24*, 1226.
[26] a) S. S. Farvid, T. Wang, P. V. Radovanovic, *J. Am. Chem. Soc.* **2011**, *133*, 6711; b) Y.-S. Fu, X.-W. Du, S. A. Kulinich, J.-S. Qiu, W.-J. Qin, R. Li, J. Sun, J. Liu, *J. Am. Chem. Soc.* **2011**, *133*, 16029.
[27] C.-C. Huang, K.-Y. Chuang, C.-P. Chou, M.-T. Wu, H.-S. Sheu, D.-B. Shieh, C.-Y. Tsai, C.-H. Su, H.-Y. Lei, C.-S. Yeh, *J. Mater. Chem.* **2011**, *21*, 7472.
[28] C.-C. Huang, C.-Y. Tsai, H.-S. Sheu, K.-Y. Chuang, C.-H. Su, U.-S. Jeng, F.-Y. Cheng, C.-H. Su, H.-Y. Lei, C.-S. Yeh, *ACS Nano* **2011**, *5*, 3905.
[29] C.-C. Huang, W. Huang, C.-S. Yeh, *Biomaterials* **2011**, *32*, 556. 4.
[30] T. Zhang, J. Ge, Y. Hu, Y. Yin, *Nano Lett.* **2007**, *7*, 3203.
[31] C.-T. Lai, J.-L. Hong, *J. Phys. Chem. C* **2009**, *113*, 18578.